J Therm Anal Calorim (2011) 103:597–606
DOI 10.1007/s10973-010-1007-2

Physicochemical properties of non-stoichiometric oxides

Mixed conductors: Part I

A. Caneiro · L. Mogni · N. Grunbaum · F. Prado

Received: 18 May 2010 / Accepted: 5 August 2010 / Published online: 29 August 2010
© Akadémiai Kiadó, Budapest, Hungary 2010

Abstract This is the first part of a review devoted to present the physicochemical properties of non-stoichiometric oxides that exhibit simultaneously ionic and electronic conductivity. Oxides mixed conductors are candidates to be used in electrochemical applications such as oxygen separation membranes, Solid Oxide Fuel Cells (SOFC) and Solid Oxide Electrolysis Cell (SOEC). In the present article, divide in two parts, we review the thermodynamic and transport properties of mixed conductors systems. In Part I is presented the layered mixed conductors $Sr_3FeMO_{6+\delta}$ (M = Fe, Co, Ni) belonging to the $n = 2$ member of the Ruddlesden–Popper series $A_{n+1}B_nO_{3n+1}$, while in Part II we discuss results obtained for the $Sr_{1-x}La_xFe_{0.2}Co_{0.8}O_{3-\delta}$ perovskites. These perovskite related intergrowth oxides, $Sr_3FeMO_{6+\delta}$, intercalate rock-salt layers in the perovskite structure decreasing the tendency of structural transformation at high temperature. The defect structure of these materials has been determined by thermodynamic measurements of the oxygen chemical potential (μO_2) as a function of oxygen content and temperature. The knowledge of the defect structure has shown to be essential to analyze electrical resistivity measurements and neutron powder diffraction data at high temperature to propose mechanisms for the electronic and ionic transport.

Keywords Mixed conductors · Ruddlesden Popper phases · Defect structure · Thermodynamical properties · Neutron diffraction

A. Caneiro (✉) · L. Mogni · N. Grunbaum · F. Prado
Centro Atómico Bariloche, CNEA, 8400 San Carlos de Bariloche, Argentina
e-mail: caneiro@cab.cnea.gov.ar

A. Caneiro
CNEA—Comisión Nacional de Energía Atómica-Argentina, Centro Atómico Bariloche, San Carlos de Bariloche, Argentina

A. Caneiro · L. Mogni
CONICET—Consejo Nacional de Investigaciones Científicas y Técnicas, Centro Atómico Bariloche, San Carlos de Bariloche, Argentina

F. Prado
CONICET—Consejo Nacional de Investigaciones Científicas y Técnicas, Universidad Nacional de Sur, Bahía Blanca, Argentina

Introduction

The no-stoichiometry in oxides can be related to the presence of cationic or anionic defects through the formation of interstitials or vacancies in the crystal structure. These point defects in the lattice modify the transport and magnetic properties of these oxides making them suitable for technological applications. The current study is the first part of a review devoted to those non-stoichiometric oxides whose defect structure allows the presence of ionic and electronic conductivity, simultaneously. In a previous review, we presented another family of non-stoichiometric oxides and their relation with the superconducting properties [1].

The mixed conductivity is an attractive property for high temperature electrochemical devices such as Solid Oxide Fuel Cell (SOFC) [2], Solid Oxide Electrolysis Cell (SOEC) or oxygen separation membranes [3]. Mixed conductivity gives the possibility of having the electrons needed for the charge transfer process and the ions for mass transfer process in the same material.

The increasing energetic demand and the poor utilization of natural resources have stimulated the search of innovative solutions either producing new fuels or using them

efficiently. In this context, the main idea of using H_2 as an energy vector has received much attention due to its high energy/mass relationship. However, there are still fundamental problems to solve. One of them is the efficient production of high purity hydrogen. In this sense, the collection of H_2 through High Temperature Steam Electrolysis (HTSE) and not by hydrocarbons reforming is presented as a possible alternative due to that the emission of both, pollutants such as NO_x and greenhouse gases like CO_2, will be prevented [4]. The HTSE has the advantage of a process free of CO and that the reaction is favored thermodynamically and kinetically with respect to the electrolysis at room temperature [5]. Recent studies showed that H_2 can be obtained using the technology of the SOEC at competitive prices [6].

Another approach to the problem of the poor use of natural resources is to use conventional fuels such as natural gas or methane in devices capable of increasing the fuel/energy conversion efficiency. The fuel cells are presented as an attractive alternative because they can achieve high efficiencies, while the theoretical values are close to 100%, the efficiencies achieved in actual devices are higher than 50% and values up to 70% in the case of using co-generation gas turbines were reported [7]. These efficiencies are significantly better than those of heat engines, whose performance range between 20 and 30%. Other advantages of the fuel cells are the possibility of built up by modular assemblage, the absence of noise and pollutant emission levels orders of magnitude lower than those of conventional power generators. Basically, fuel cells are electrochemical devices that convert chemical energy stored in a fuel directly into electrical power. Among the various types of fuel cells, the Polymer Electrolyte Membrane fuel cell (PEM) using a polymer as electrolyte and operating temperatures near 353 K, and the SOFC, with solid oxide electrolytes and operating temperatures above 973 K have attracted a lot of interest. The main advantage of the SOFC is its greater flexibility from the fuel point of view, since it can produce electrical energy either from hydrogen or hydrocarbons [8, 9]. The high operating temperature of the SOFC eliminates the use of precious metals as electrodes, but poses severe challenges for the construction of durable devices.

The SOEC basically can be thought as a SOFC, working in reverse mode [5]. Therefore, many materials currently studied as potential candidates for SOFC cathode can also be used as anodes in the SOEC.

While the solid oxide cell are efficient systems for energy conversion and production of H_2, the oxygen separation membranes are oxides ceramics with selectivity for the oxygen diffusion allowing the control of oxygen partial pressure in reactivity chambers for selective oxidation of hydrocarbons [3]. Particularly, mixed conductors with high oxide-ion conductivity can be used as oxygen separation membranes without the use of electrodes and external circuit required for a traditional ceramic oxygen pump.

Materials selection for these high temperature electrochemical devices involves an iterative design process that eventually becomes specific to the technical requirements and economic considerations. By one hand, in SOCs the critical parameters to the efficiency and operation are the voltages loss associated to ohmic drop in electrolyte and overpotentials on electrodes. By other hand, in oxygen separation membranes the critical issue is the stability of the ceramic membranes in both oxidant and reducing atmospheres. Besides, long term stability is required for both electrochemical devices due to the high working temperature. Therefore, thermodynamic and structural stability, along with chemical compatibility and zero thermal stress should be assured for the materials.

Most of the mixed conductors to be used as potential candidates for oxygen electrodes of intermediate temperature SOCs and oxygen separation membranes are transition metal oxides with perovskite or perovskite-related crystal structures exhibiting oxygen non-stoichiometry. The electronic conductivity of mixed conductors is mainly related to the mixed valence of the transition metals whereas the ionic conductivity is due to the presence of mobile oxygen vacancies at high temperatures.

It seems evident that the electrode reaction in oxygen electrodes and the oxygen transport in ceramic membranes should be related to the defect structure of the transition metal oxides.

The thermal analysis involves powerful techniques allowing the evaluation of the defect structure [10–14] and structural transformations [15, 16] of non-stoichiometric oxides used in combination with data obtained from high temperature XRD. Also it is possible to study, trough thermal analysis, the thermodynamic properties, and the chemical stability of diverse systems [17, 18].

In this article, divide in two articles; we revise the thermodynamic, transport properties and structural stability of two mixed conductors systems for SOCs oxygen electrodes and oxygen separation membranes. We studied the nature of the defect structure by means of thermogravimetric (TG) and electrical resistivity measurements under atmospheres with controlled oxygen partial pressure (pO_2). Also, we analyzed the phase stabilities combining TG with high temperature X-Ray and Neutron diffraction. Part I is focused on the $n = 2$ $Sr_3FeMO_{6+\delta}$ (M = Fe, Co, Ni) Ruddlesden–Popper phases, while in Part II is discussed the results obtained for the solid solution $Sr_{1-x}La_xFe_{0.2}Co_{0.8}O_{3-\delta}$ perovskite with $0 \leq x \leq 0.4$. We will show that accurate thermogravimetric measurements under controlled $p(O_2)$ allow the determination of the partial molar properties: the oxygen chemical potential μO_2; the partial molar entropy s_{O_2}; and the partial molar enthalpy h_{O_2}. These

thermodynamic properties provide useful information not only of the lattice defects but also of the electronic defects. In the case of the R–P phases, the defect structure determined from thermodynamic measurements was confirmed by electrical resistivity measurements and neutron powder diffraction data.

Experimental

Samples of the $n = 2$ R–P compounds $Sr_3Fe_2O_{6+\delta}$, $Sr_3FeCoO_{6+\delta}$, $Sr_3FeNiO_{6+\delta}$ were synthesized by an acetic-based gel route.

For the $Sr_3Fe_2O_{6+\delta}$, $Sr_3FeCoO_{6+\delta}$, $Sr_3FeNiO_{6+\delta}$ compounds, stoichiometric quantities Fe, Ni, and Co acetates and $SrCO_3$ were dissolved in acetic acid and refluxed for 2 h. The solution was then heated in a hot plate to form a dark red transparent gel. This gel was dried and decomposed at 723 K for 30 min in air. An intermediate heat treatment was performed at 1223 K for 12 h in air. Dense samples were obtained by pressing the powders into pellets with a final heat treatment at 1573 K under pure O_2 for 20 h.

The presence of single phase materials, with tetragonal symmetry (S.G. *I*4/mmm) for $Sr_3FeMO_{6+\delta}$ was checked by powder XRD. No evidence of secondary phases was detected for both materials. The homogeneity of the samples was confirmed by SEM observations and EDS analysis.

Themogavimetric measurements (TG) under controlled $p(O_2)$ were performed using a highly sensitive thermogravimetric equipment [19, 20] consisting of a symmetrical thermobalance based on a Cahn 1000 electrobalance coupled to an electrochemical gas blending system. The electrochemical system is composed of an electrochemical oxygen pump and an oxygen sensor. The electrochemical pump provides Ar–O_2 mixtures and the oxygen sensor determine the $p(O_2)$. Mixtures of Ar-O_2 with $p(O_2)$ within the range $10^{-5} < p(O_2) < 1$ atm can be easily prepared by only changing the electrical current applied to the oxygen pump.

The thermobalance allows the determination of sample mass changes within ± 10 μg, i.e., for oxide samples of about 0.6 g of $Sr_3(FeM)O_{6+\delta}$, changes on the oxygen content within ± 0.0003 can be detected.

The equilibrium criterion used for our measurements, verified over a period of 24 h, was constant mass samples within 10 mg. A more detailed description of this thermobalance can be found in [1].

After performing the TG measurements under controlled $p(O_2)$, the absolute oxygen content of the samples were determined in situ by reduction in dry H_2 at 1273 K. SrO and metallic Co, Fe, or Ni were the final products depending on the composition of the compound.

DC resistivity measurements at high temperature and controlled $p(O_2)$ were carried out by a standard four-probe method on rectangular samples with dimensions 1.5 mm × 5 mm × 20 mm.

Neutron powder diffraction patterns were recorded at the Institute Laue-Langevin, Grenoble-France, on the D2B powder diffractometer at $T = 293$, 573, 773, 973, and 1173 K. Data were collected using the wavelength $\lambda = 1.594$ Å, in the angular range $10° \leq 2\theta \leq 140°$ with steps of 0.05°. At room temperature, the samples were handled under flowing He and placed in a vanadium can. For NPD measurements at $T \geq 573$ K, the samples were placed in a quartz tube open at the top in contact with air.

Results and discussion

In Fig. 1 the crystal structures of the $n = 2$ R–P phases $Sr_3(Fe,M)O_{6+\delta}$ (M = Fe, Co, Ni) is shown. The crystal structure of the $n = 2$ R–P phases ($A_3B_2O_7$) consists of an ordered sequence of two perovskite layers ABO_3 alternating with rock-salt layer AO along the *c*-axis [21, 22].

$Sr_3FeMO_{6+\delta}$ (M = Fe, Co, Ni) Thermodynamic properties

The $n = 2$ R–P phases $Sr_3FeMO_{6+\delta}$ (M = Fe, Co, Ni) are candidates for high temperature electrochemical applications since the presence of mixed conductivity has been reported for some compositions [23–25]. These materials present better themodynamic stability than cobaltites with perovskite structure and do not exhibit any phase transition within the working temperature and $p(O_2)$ ranges used for

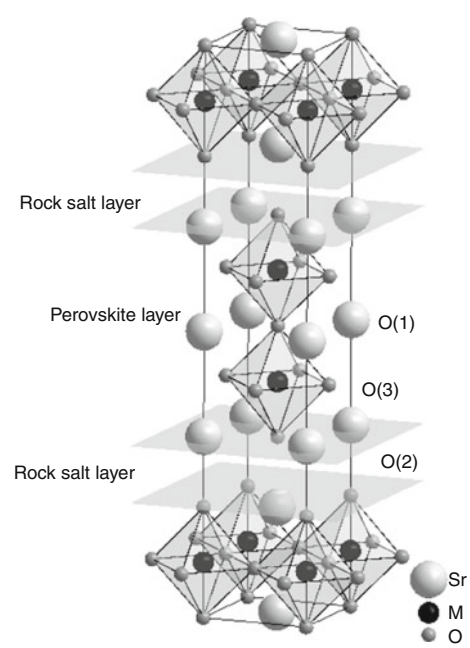

Fig. 1 Crystal structure of the $n = 2$ $Sr_3FeMO_{6+\delta}$ (M = Fe, Co, Ni) Ruddlesden–Popper phase (S.G. I4/mmm)

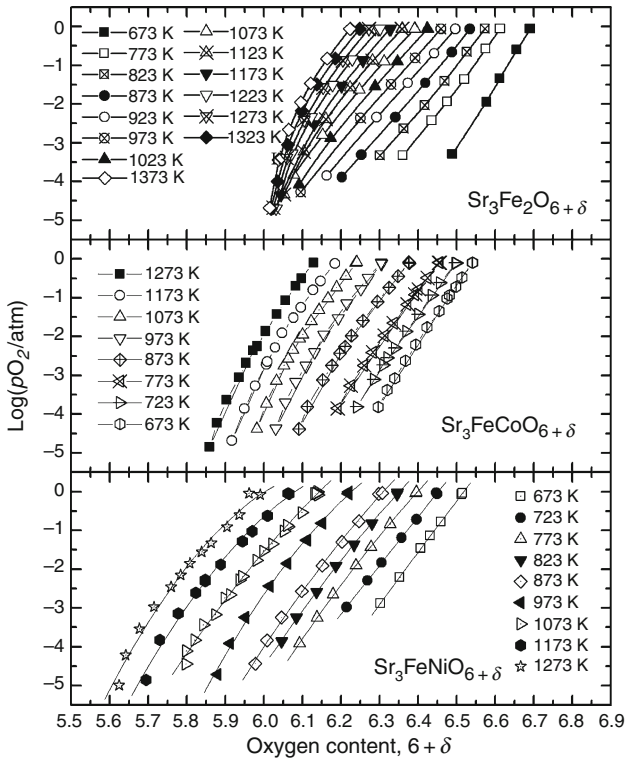

Fig. 2 Isotherms of log $p(O_2)$ vs. oxygen content "6+δ" for $Sr_3Fe_2O_{6+\delta}$, $Sr_3FeCoO_{6+\delta}$ and $Sr_3FeNiO_{6+\delta}$ at several temperatures [26, 27]

electrochemical applications. In Fig. 2 the isotherms of the equilibrium $p(O_2)$ as a function of the oxygen content for the $Sr_3FeMO_{6+\delta}$ (M = Fe, Co, Ni) compounds at several temperatures are plotted. These compounds display a wide range of oxygen non-stoichiometry and the isotherms do not present any plateau characteristic of a phase transition, within the range of measurements.

From the equilibrium $p(O_2)$ data, the oxygen chemical potential, μ_{O_2}, can be computed using the following equation:

$$\mu_{O_2} = \mu_{O_2}^{oxide} = \mu_{O_2}^{ref} + RT \ln p(O_2)/p(O_2)^{ref}) \quad (1)$$

where R is the gas constant, $p(O_2)^{ref} = 1$ atm and $\mu_{O_2}^{ref}$ the oxygen chemical potential of the reference gas obtained from themodynamic tables [28].

From the μ_{O_2} data, the partial molar enthalpy h_{O_2} and the partial molar entropy s_{O_2} can be determined by means of the following relations:

$$s_{O_2} = -\left.\frac{\partial \mu_{O_2}}{\partial T}\right|_{\delta}, \quad (2)$$

$$h_{O_2} = \left.\frac{\partial(\mu_{O_2}/T)}{\partial(1/T)}\right|_{\delta} \quad (3)$$

The values of s_{O_2} and h_{O_2} for the R–P phases are displayed in Figs. 3, 4, 5, and 6 and the result are discussed in next sections.

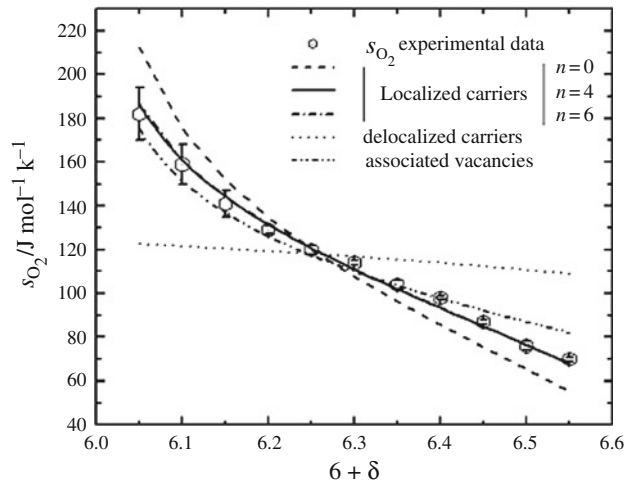

Fig. 3 Partial molar entropy, s_{O_2}, as a function of oxygen content "6+δ" for $Sr_3Fe_2O_{6+\delta}$. The *lines* represent the fitting with different defects models [26]. At high oxygen content the *errors bars* are lower than symbol size

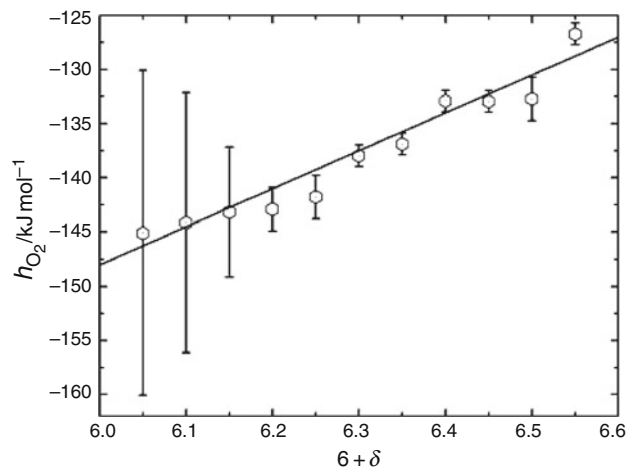

Fig. 4 Partial molar enthalpy, h_{O_2} as a function of oxygen content "6+δ" for $Sr_3Fe_2O_{6+}$ [24]

$Sr_3Fe_2O_{6+\delta}$

At high temperatures and low values of $p(O_2)$ the oxygen content of the $Sr_3Fe_2O_{6+\delta}$ compound tends to the value 6.00 indicating the stabilization of $Sr_3Fe_2O_6$ with all Fe as 3+. In Figs. 3 and 4, the s_{O_2} and h_{O_2} values, respectively, as a function of oxygen content "6+δ" for $Sr_3Fe_2O_{6+\delta}$ are shown. These values were determined using Eqs. 2 and 3. Both thermodynamic quantities were fitted in the frame of the regular solution model with defect models considering either localized charge carriers in the Fe sites [29–33] or itinerant carriers [34–36].

The defect equation in the Kröger–Vink notation for localized charge carrier is the following:

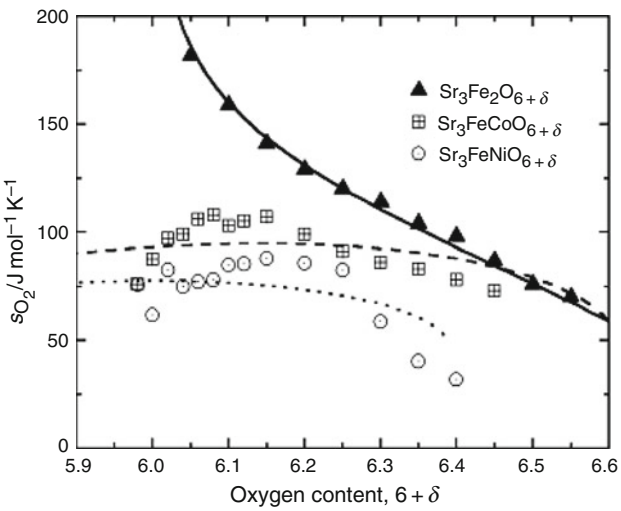

Fig. 5 s_{O_2} vs. oxygen content "6+δ" for $Sr_3FeCoO_{6+\delta}$ and $Sr_3FeNiO_{6+\delta}$. The *lines* represent the fitting of the data with a defect model involving localized and itinerant charge carriers. The s_{O_2} data for $Sr_3FeCoO_{6+\delta}$ have been included for comparison [27]

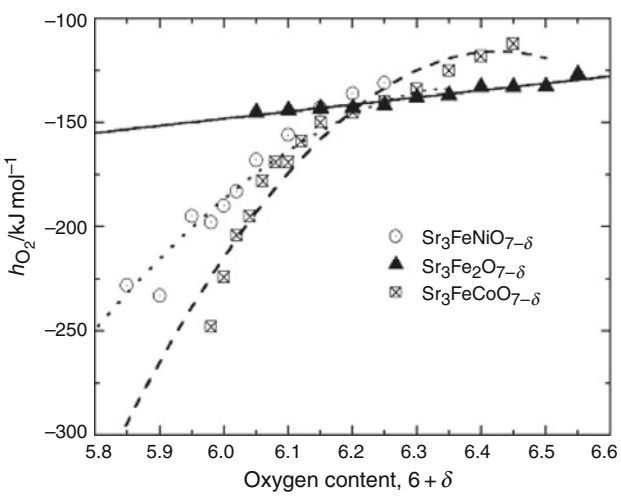

Fig. 6 h_{O_2} vs. oxygen content "6+δ" for $Sr_3FeCoO_{6+\delta}$, $Sr_3FeNiO_{6+\delta}$. The *lines* represent the fitting of the data with a defect model involving localized and itinerant charge carriers. The h_{O_2} data for $Sr_3FeCoO_{6+\delta}$ have been included for comparison [27]

$$V_O^{\bullet\bullet} + \frac{1}{2}O_2 + 2Fe_{Fe}^x \leftrightarrow O_O^x + 2Fe_{Fe}^{\bullet} \quad (4)$$

where $V_O^{\bullet\bullet}$ represents double charged oxygen vacancies, O_O^x is a double charged oxygen ion (O^{2-}) in the crystal lattice sites O(1), O(2), and O(3). Finally, Fe_{Fe}^x and $Fe_{Fe}^{\bullet}$ denote the cations Fe^{3+} and Fe^{4+}, respectively, in the Fe crystallographic sites.

For itinerant carriers the defect equation is:

$$V_O^{\bullet\bullet} + \frac{1}{2}O_2 + 2e' \leftrightarrow O_O^x \quad (5)$$

where e' represents an electron in the conduction band.

The partial molar properties s_{O_2} and h_{O_2} can be calculated from defect Eqs. 4 and 5 considering ideal mixing entropy, the crystal site balance and the charge neutrality condition. For localized charge carriers the expression for s_{O_2} is:

$$s_{O_2} = -2s_V^0 - 4s_{Fe}^0 - 2R\ln\frac{(n+\delta)\delta^2}{(1-\delta)} \quad (6)$$

where s_V^0 and s_{Fe}^0 are constants corresponding to the standard entropy of the oxygen and electronic defects and n is a parameter that takes different values depending on the oxygen crystal sites involved in the computation of the mixing entropy. Thus, n equals 0 for O(1), 4 for O(1) and O(3) and 6 for O(1), O(2) and O(3).

In this model both, the oxygen defects and the localized charge carriers, contribute to the partial molar entropy; contrary to the case of the defect Eq. 5 where only the oxygen defects contribute to s_{O_2}.

In Fig. 3 the experimental data for s_{O_2} and the fitting with different defect models are shown.

A great difference in the fitting for models considering localized or itinerant charge carriers can be observed. It is clear from this fitting that the s_{O_2} data strongly suggest the presence of localized charge carriers in the Fe sites for the $Sr_3Fe_2O_{6+\delta}$ compound. The fitting of s_{O_2} is also improved considering the presence of vacancies not only in the O(1) site but also in the O(3) and O(2) sites. The fitting does not differentiate between oxygen vacancies in the O(1) and O(3), and O(1), O(2), and O(3) crystal sites.

The expression for h_{O_2} considering the defect Eq. 4 is:

$$h_{O_2} = -2h_V^0 - 4h_{Fe}^0 + 2a\delta, \text{ with } a = RT\ln\frac{\gamma_{O_O^x}\gamma_{Fe_{Fe}^{\bullet}}^2}{\gamma_{V_O^{\bullet\bullet}}\gamma_{Fe_{Fe}^x}^2} \quad (7)$$

where h_V^0 and γh_{Fe}^0 are the standard molar enthalpy of oxygen and electronic defects, respectively. $\gamma_{O_O^x}, \gamma_{Fe_{Fe}^{\bullet}}^2, \gamma_{V_O^{\bullet\bullet}}\gamma_{Fe_{Fe}^x}^2$ are the activity coefficients of O_O^x, $Fe_{Fe}^{\bullet}$, $V_O^{\bullet\bullet}$, and Fe_{Fe}^x, respectively.

The experimental data for h_{O_2} plotted in Fig. 4 show a slightly linear dependence of h_{O_2} on 6+δ. This fact indicates the presence of defect interactions in the $Sr_3Fe_2O_{6+\delta}$ compound and therefore a deviation of h_{O_2} from the ideal solution model.

From the linear fitting of the experimental data shown in Fig. 4, we have obtained the value of the parameter $a = 17$ (2) kJ $\times$ mol^{-2}, which is related to the defect interactions through the values of the activity coefficients γ_i. This value is one order of magnitude lower than those obtained by Osuma et al. for the $La_{1-x}Ca_xCrO_{3-\delta}$ perovskite [32] indicating weaker defect interactions for $Sr_3Fe_2O_{6+\delta}$.

The good fitting of the s_{O_2} data, considering a random distribution of point defects and the low values of the

parameter "a", suggest that the defect interactions are weak enough to prevent defect association (clusters) or ordering [37]. This behavior differs from that observed for $SrFe_{0.2}Co_{0.8}O_{3-\delta}$ where the high h_{O_2} values suggest a strong interaction among defects. A detailed discussion about these results can be found in ref [26].

$Sr_3FeNiO_{6+\delta}$ and $Sr_3FeCoO_{6+\delta}$

In Figs. 5 and 6, s_{O_2} and h_{O_2} data as a function of oxygen content "$6+\delta$" for $Sr_3FeNiO_{6+\delta}$ and $Sr_3FeCoO_{6+\delta}$ are plotted. For comparison, the data of $Sr_3Fe_2O_{6+\delta}$ are included. The behavior of both s_{O_2} and h_{O_2} for $Sr_3FeNiO_{6+\delta}$ and $Sr_3FeCoO_{6+\delta}$ differs qualitatively from those obtained for $Sr_3Fe_2O_{6+\delta}$ suggesting a different defect structure.

In particular the slight dependence of s_{O_2} with $6+\delta$ for $Sr_3FeNiO_{6+\delta}$ and $Sr_3FeCoO_{6+\delta}$, similar to that plotted in Fig. 3 for itinerant charge carriers, strongly suggests the presence of delocalized electronic defects.

It is well known that the presence of localized charge carriers is a common feature of the $(La,Sr)FeO_{3-\delta}$ perovskites [29–31]. The situation is completely different for $(La,Sr)CoO_{3-\delta}$ perovskites, where the delocalized charge carriers are distributed in a partial filled Co(3d)–O(2p) band [35, 36]. Therefore, similarly to that proposed by Lankhorst et al. [35] for the $La_{0.6}Sr_{0.4}Co_{1-y}Fe_yO_{3-\delta}$ perovskite, we have considered for $Sr_3FeNiO_{6+\delta}$ and $Sr_3FeCoO_{6+\delta}$ a defect model linking Eqs. 4 and 5. A fraction f_e of the electrons involved in the defect reaction is taken from the M(3d)–O(2p) (M = Ni, Co) conduction band, whereas the remaining $1 - f_e$ fraction of electrons is distributed in the localized states of the iron sites.

The defect reaction for this model:

$$2V_O^{\bullet\bullet} + O_2 + 4(1-f_e)Fe_{Fe}^x + 4f_e e' \leftrightarrow 2O_O^x + 4(1-f_e)Fe_{Fe}^{\bullet} \quad (8)$$

The model considers an equilibrium exchange reaction of charge carriers between the M(3d)–O(2p) (M = Co, Ni) conduction band and localized iron states:

$$Fe_{Fe}^{\bullet} + 2e' \leftrightarrow Fe_{Fe}^x \quad (9)$$

Taking into account the low value of the interaction parameter "a" determined for the $Sr_3Fe_2O_{6+\delta}$ compound, it is plausible to considerer that in the Ni and Co substituted compounds the defects ($V_O^{\bullet\bullet}$, O_O^x, and Fe_{Fe}^x, $Fe_{Fe}^{\bullet}$) are randomly distributed in the oxygen and iron lattice sites and the interaction between defects can be neglected. Besides, the chemical potential of the charge carriers in the conduction band mainly contributes to h_{O_2} and can be expressed using the rigid band model formalism [35, 36]:

$$\mu_{e'} = \mu_{e'}^0(T) + \frac{[e'] - [e']^0}{g(E_F)[M]} \quad (10)$$

where $\mu_{e'}^0(T)$ denotes the chemical potential of the standard state ($\delta = 1$), $[e']$ is the electron occupancy, $[e']^0$ is the electron occupancy for the standard state, $g(E_F)$ is the density of states at the Fermi level for the standard compound and, $[M]$ is the concentration of the transition metal (Co or Ni); which is equal to 1 in this case.

Therefore, expressions for s_{O_2} and h_{O_2} can be obtained by replacing the chemical potentials in the equilibrium reactions (4) and (5), and considering the oxygen crystallographic site balance, the iron sites balance, the charge neutrality condition and the equilibrium and boundary conditions. From the fitting of experimental data of s_{O_2} and h_{O_2} with these expressions, it is possible to evaluate the fraction of localized and delocalized charge carriers as a function of oxygen content. A detailed description of this model used to fit the s_{O_2} and h_{O_2} data can be found in Ref [27].

In Figs. 5 and 6 the results of this fitting are presented. It is worth mentioning that a simple model considering localized charge carriers in the Fe sites in addition to itinerant charge carriers in a rigid M(3d)–O(2p) band, allows a realistic fitting of both thermodynamic quantities. The presence of delocalized charge carriers releases the singularity found in s_{O_2} as $6+\delta$ approaches to 6.00 for $Sr_3Fe_2O_{6+\delta}$. The rapid variation of h_{O_2} observed at lower oxygen content for both $Sr_3FeNiO_{6+\delta}$ and $Sr_3FeCoO_{6+\delta}$ compounds is mainly related to the contribution of the chemical potential of the delocalized charge carriers in the Ni and Co bands.

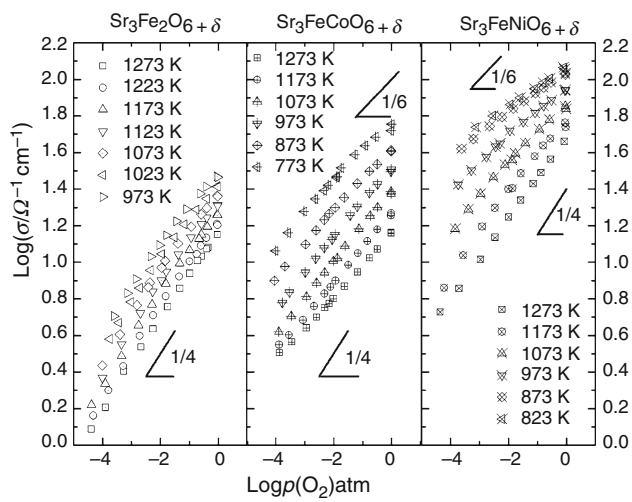

Fig. 7 Isotherms of the electrical conductivity as a function of log $p(O_2)$ for $Sr_3Fe_2O_{6+\delta}$, $Sr_3FeCoO_{6+\delta}$, and $Sr_3FeNiO_{6+\delta}$ compounds [27]

$Sr_3FeMO_{6+\delta}$ (M = Fe, Co, Ni) electrical conductivity

In Fig. 7 isotherms of the electrical conductivity as a function of $p(O_2)$ for $Sr_3Fe_2O_{6+\delta}$, $Sr_3FeCoO_{6+\delta}$, and $Sr_3FeNiO_{6+\delta}$ in a log–log plot are presented. The electrical conductivity increases according to the series Fe < Co < Ni. The three compounds present a positive slope of log σ vs. log $p(O_2)$. This fact suggests the presence of p type charge carriers. The log σ vs. log $p(O_2)$ slope is close to ¼ for $Sr_3Fe_2O_{6+\delta}$ at high temperatures and low $p(O_2)$. In this limit $\sigma \propto [Fe^{\bullet}_{Fe}] \propto p(O_2)^{1/4}$. The slopes log σ vs. log $p(O_2)$ for $Sr_3FeCoO_{6+\delta}$ and $Sr_3FeNiO_{6+\delta}$ are lower than ¼. The presence of itinerant charge carriers in addition to localized ones in both $Sr_3FeCoO_{6+\delta}$ and $Sr_3FeNiO_{6+\delta}$ compounds should be the responsible of this behavior.

Valuable information on the mechanism involved in the electrical conductivity can be extracted from the dependence of the electrical conductivity as a function of the oxygen content or charge carrier concentration. In order to obtain these data it is necessary to combine the log σ vs. log $p(O_2)$ data shown in Fig. 7 with log $p(O_2)$ vs. oxygen content data shown in Fig. 2.

In Fig. 8 the electrical conductivity "σ" vs. oxygen content "6+δ" at different temperatures for the $Sr_3FeMO_{6+\delta}$ (M = Fe, Co, Ni) compounds are plotted. For the three compounds σ is thermally activated and increases with the series $Sr_3Fe_2O_{6+\delta} < Sr_3FeCoO_{6+\delta} < Sr_3FeNiO_{6+\delta}$ at a fixed oxygen content value. This trend is in agreement with the enhanced covalence of the M–O bonding from the left to the right in the transition metal series.

The electrical conductivity is given by:

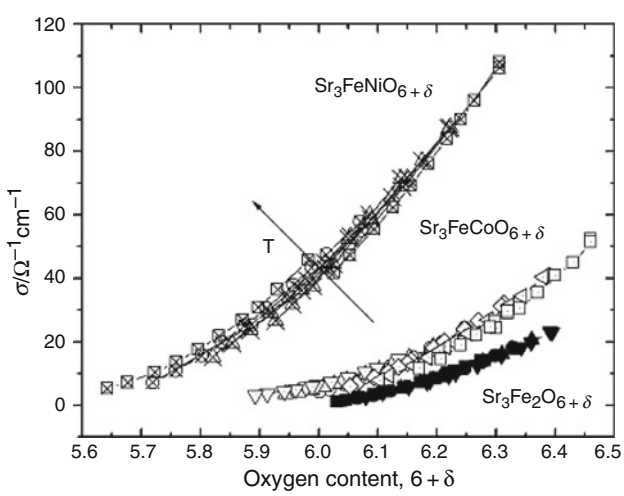

Fig. 8 Electrical conductivity σ as a function of 6+δ for $Sr_3Fe_2O_{6+\delta}$, $Sr_3FeCoO_{6+\delta}$, and $Sr_3FeNiO_{6+\delta}$ compounds at several temperatures [27]. The *arrow* indicates how T increases

$$\sigma_p = [X_p] e \mu_p \quad (11)$$

where $[X_p]$ is the p-carriers concentration, e the electron charge, and μ the mobility of the charge carrier.

Therefore, the thermal activated behavior of the electrical conductivity could be associated to any of the following mechanisms: (a) small polaron conductivity mechanism (μ increase with T), (b) semiconductor or large polaron behavior (X_p increases with T) [38–41].

For the $Sr_3Fe_2O_{6+\delta}$ compound, μ_p can be easily estimated from Eq. 11 since the holes are localized at the Fe crystal sites as $Fe^{\bullet}_{Fe}$, and therefore the charge carriers concentration is given by $[X_p] = \frac{2\times 2\delta}{V_{c.u.}}$ where $V_{c.u.}$ is the volume of the unit cell. Thus, μ_p varies between 0.015 and 0.03 $cm^2\ V^{-1}\ s^{-1}$ for $6.1 < 6+\delta < 6.5$. These low mobility values are typically found in those material where the mechanism for electrical conductivity is dominated by small polarons. In the small polaron model the charge carriers have a strong interaction with the lattice and they are localized on the crystal sites (Fe in this case). Consequently, the charge carriers jump through the lattice with a thermal activated mobility.

If the small polaron model is assumed in the case of substituted compounds, the estimated mobility values are in the range of $1.12 \geq \mu_p^{LP} \geq 0.27\ cm^2\ V^{-1}\ seg^{-1}$ within the interval 6.00 < "6+δ" < 6.3 for $Sr_3FeCoO_{6+\delta}$ and $1.82 \geq \mu_p^{LP} \geq 0.68\ cm^2\ V^{-1}\ seg^{-1}$ between 5.8 < "6+δ" < 6.2 for $Sr_3FeNiO_{6+\delta}$. These mobility values are higher than the typical ones of the small polaron model which are generally between 10^{-4} and $10^{-1}\ cm^2\ V^{-1}\ s^{-1}$.

In this case, the electrical conductivity behavior could be understood considering the large polaron model where the charge-carrier/phonon interaction is weaker than that of small polaron. In addition, the charge carriers move in a conduction band with a large effective mass due to the drag of their polarization cloud. Thus, the electrical conductivity presents a thermally activated behavior mainly due to the large polaron energy formation E_f. In this frame, the charge carriers are not localized in the crystal lattice and consequently they do not contribute to the configurational entropy in agreement with that deduced above from the partial molar properties. Besides, the mobility values for large polarons are generally within the range 1–10 $cm^2\ V^{-1}\ s^{-1}$. Considering this large polaron model it is possible to recalculate the mobility values taking into account the defect model discussed before for the Co and Ni substituted compound.

In this case, the concentration of the delocalized charge carriers could be estimated by the computation of the defect concentration using the defect model and the E_f values obtained from the conductivity data. On the other hand, the contribution of localized charge in the Fe sites to the total

electrical conductivity has been neglected. Thus, for the delocalized charge carriers in the $Sr_3FeCoO_{6+\delta}$ compound, mobility values of $0.46 \geq \mu_p^{LP} \geq 0.10$ cm^2 V^{-1} seg^{-1} within the interval $6.00 <$ "$6+\delta$" < 6.3 and for $Sr_3FeNiO_{6+\delta}$ $0.31 \geq \mu_p^{LP} \geq 0.21$ cm^2 V^{-1} seg^{-1} between $5.8 <$ "$6+\delta$" < 6.2 are obtained.

These estimated mobility values for both the $Sr_3FeCoO_{6+\delta}$, and $Sr_3FeNiO_{6+\delta}$ compounds can be assigned either to a large or small polaron behavior. Consequently, it is difficult to infer the nature of the charge carriers solely from this estimation. However, the high temperature thermodynamic data, s_{O_2} and h_{O_2}, also provide information on the nature of the charge carriers as we discussed above. The charge carrier delocalisation suggested by the dependence of s_{O_2} and h_{O_2} on "$6+\delta$" data gives an additional insight for a charge carrier conduction mechanism of the Large Polaron type. A detailed discussion about these results can be found in [26] and [27].

$Sr_3FeMO_{6+\delta}$ (M: Fe, Co, Ni) neutron powder diffraction

In metal oxides, the X-ray scattering is dominated by the presence of the heavy atoms with large number of electrons. Therefore, it is very difficult to determine the occupancy factor of the oxygen crystal sites from the refinement of the crystal structure using XRD data. One way to solve this problem is to carry out Neutron Powder Diffraction (NPD) experiments.

Moreover, the use of in situ high resolution NPD allows an accurate determination of the oxygen occupancy factors at different temperatures. This information is undoubtedly essential to corroborate the oxygen defect structure deduced from the thermogravimetric measurements.

In Fig. 9 the oxygen occupancy of the O(1) (0,0,0) and O(3) (0,1/2,z) crystal sites for $Sr_3Fe_2O_{6+\delta}$, $Sr_3FeCoO_{6+\delta}$, and $Sr_3FeNiO_{6+\delta}$ determined from the crystal structure refinement using high temperature NPD data are shown. The O(2) crystal site is considered fully occupied at all

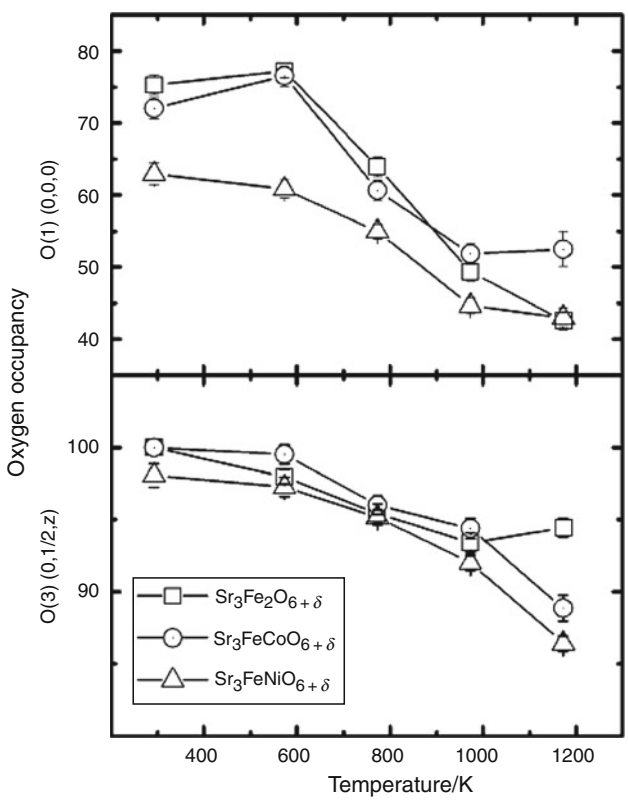

Fig. 9 Variation of the occupancy factor of the O(1) (2a, 0,0,0) and O(3) (8g,0,1/2,*z*) crystal sites with temperature in air [42]

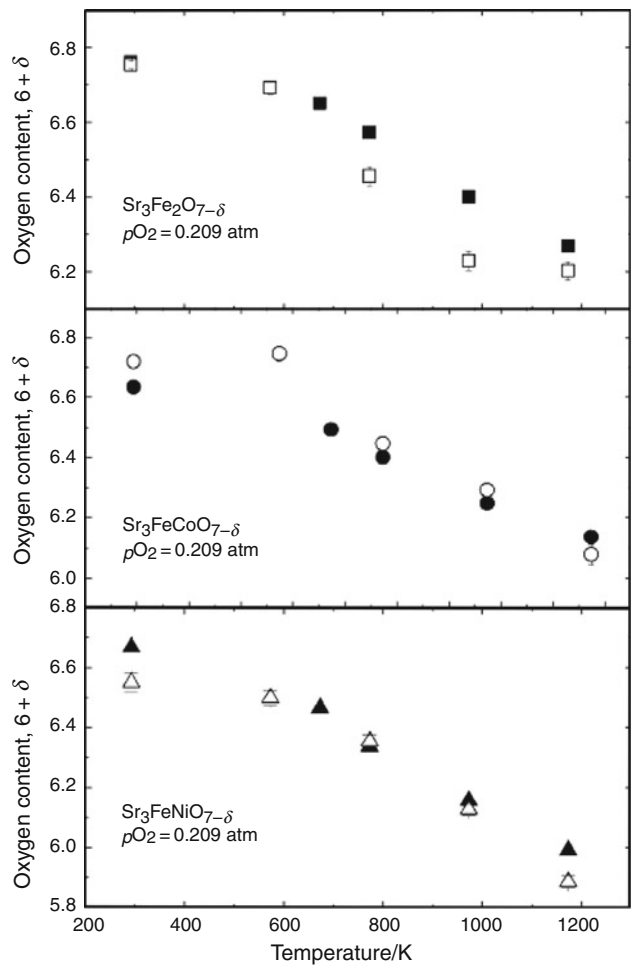

Fig. 10 Variation of the total oxygen content of the $Sr_3FeMO_{6+\delta}$ (M = Fe, Co, Ni) samples with temperature obtained from NPD data (*open symbols*) [42]. The *solid symbols* in the temperature range $673 \leq T \leq 1173$ K correspond to the oxygen content values obtained from thermogravimetric measurements of the equilibrium $p(O_2)$ at 0.209 atm [26, 27]. The oxygen content values at $T = 293$ K (*solid symbols*) were obtained by reducing the samples in dry H_2. Previously to the reduction process the samples were cooled in flowing O_2 with the same cooling rate used for the samples utilized during NPD measurements

temperatures. It can be seen that the oxygen occupancy is practically 100% at room temperature for the O(3) site, while is appreciably lower for the O(1) site. Therefore, the accommodation of oxygen non-stoichiometry at room temperature for the three compounds mainly occurs by the creation of oxygen vacancies at the O(1) site. However, the refinements of the crystal structures at high temperature indicate the presence of a non-negligible concentration of oxygen vacancies in the O(3) (8g,0,1/2,z) site in the $(Fe/M)O_2$ planes of the perovskite layers even when the total oxygen content is above 6.00.

Previous analysis of neutron powder diffraction data on $Sr_3(Fe,Co)_2O_{6+\delta}$ samples, quenched from high temperature to control the oxygen content between 6 and 7, located the oxygen vacancies only on the O(1) crystal site [22, 43]. At the same time, oxygen vacancies on the O(3) crystal site have also been reported for Sr_3FeCoO_{7-y} with $y = 1.55$ and 1.118 and $Sr_3Co_2O_{5+z}$ with $z = 0.91$, 0.64, and 0.38 [42–45]. These results were obtained from NPD data recorded at room temperature on samples with controlled oxygen content below 6.00 [43–45]. Instead, our results indicate that the crystal structure of the R–P phases $Sr_3FeMO_{6+\delta}$ (M = Fe, Co, Ni) contains oxygen vacancies on the O(3) sites when the total oxygen content is also higher than 6.00, which supports the defect model proposed for $Sr_3Fe_2O_{6+\delta}$ to reproduce thermodynamic data [26]. Furthermore, these results are in agreement with the oxide ion diffusion mechanism proposed for $Sr_3Fe_{2-x}Ti_xO_{6+\delta}$ ($0 \leq x \leq 2$) [46] and $Sr_3Fe_{2-x}Sc_xO_{6+\delta}$ ($x = 0.2$ and 0.3) [47] involving oxygen jumps from the filled O(3) crystal site to an empty O(1) position.

From the oxygen occupancy factors at the O(1) and O(3) site the oxygen content for the three compounds were determined. In Fig. 10, a comparison between the values of oxygen content determined by thermogravimetry with those obtained by NPD is presented. It can be noted that the agreement between both techniques is quite acceptable.

Conclusions

The thermodynamic properties μ_{O_2}, s_{O_2} and h_{O_2} are shown for the $n = 2$ $Sr_3(FeM)O_{6+\delta}$ (M: Fe, Co, Ni) Ruddlesden–Popper phase. The defect structure for $Sr_3Fe_2O_{6+\delta}$, $Sr_3FeCoO_{6+\delta}$, and $Sr_3FeNiO_{6+\delta}$ is evaluated through the dependence of both s_{O_2} and h_{O_2} with the oxygen content "6+δ". The behavior of s_{O_2} and h_{O_2} with "6+δ" suggests the presence of localized holes carriers for $Sr_3Fe_2O_{6+\delta}$ and itinerant charge carriers for $Sr_3FeCoO_{6+\delta}$ and $Sr_3FeNiO_{6+\delta}$. The s_{O_2} vs. oxygen content "6+δ" data for $Sr_3Fe_2O_{6+\delta}$ strongly indicates the presence of oxygen vacancies in the O(3) crystallographic site in addition to those of the O(1) site.

For $Sr_3FeCoO_{6+\delta}$ and $Sr_3FeNiO_{6+\delta}$, a fraction f_e of the electrons involved in the defect reaction is taken from the M(3d)−O(2p) (M = Ni, Co) conduction band, whereas the remaining $1 - f_e$ fraction of electrons is distributed in the localized states of the iron sites.

Electrical conductivity data for $Sr_3Fe_2O_{6+\delta}$, $Sr_3FeCoO_{6+\delta}$, and $Sr_3FeNiO_{6+\delta}$ as a function of pO_2 and oxygen content "6+δ" support the defect structure inferred from thermodynamic data.

NPD data confirm the presence of oxygen vacancies in the O(3) site in agreement with that suggested from s_{O_2} vs. "6+δ".

Acknowledgements This study was supported by CNEA (Argentine Atomic Energy Commission), CONICET, Agencia-FONCyT, and Universidad Nacional de Cuyo.

References

1. Caneiro A, Prado F, Serquis A. Physical properties of non-stoichiometrics oxides: superconducting oxides. J Therm Anal Calorim. 2006;83(2):507–18.
2. Brandon NP, Skinner S, Steele BCH. Recent advances in materials for fuel cells. Annu Rev Mater Res. 2003;33:183–213.
3. Kharton VV, Yaremchenko AA, Kovalevsky AV, Viskup AP, Naumovich EN, Kerko PF. Perovskite-type oxides for high-temperature oxygen separation membranes. J Memb Sci. 1999; 163:307–17.
4. Ghenciu A. Review of fuel processing catalysts for hydrogen production in PEM fuel cell systems. Curr Opin Solid State Mater Sci. 2002;6:389–99.
5. Brisse A, Schefold J, Zahid M. High temperature water electrolysis in solid oxide cells. Int J Hydrog Energy. 2008;33: 5375–82.
6. Jensen S, Larsen P, Mogensen M. Hydrogen and synthetic fuel production from renewable energy sources. Int J Hydrog Energy. 2007;21:3253–7.
7. Larminie J, Dicks A. Fuel cells systems explained. 2nd ed. Chichester: Wiley; 2003.
8. Steel BCH, Heinzel A. Materials for fuel-cell technologies. Nature. 2001;414:345–52.
9. Song C. Fuel processing for low-temperature and high-temperature fuel cells: challenges, and opportunities for sustainable development in the 21st century. Catal Today. 2002;77:17–49.
10. González Arias A, Torres C, de Francisco C, Muñoz JM, Hernández Gómez P, Alejos O, Montero O, Iñiguez JI. Defect concentration in Ti-substituted YIG from TG curves. J Therm Anal Calorim. 2006;86(1):195–8.
11. Grzesik Z, Mrowec S. Kinetics and thermodynamics of point defects in non-stoichiometric metal oxides and sulphides. J Therm Anal Calorim. 2007;90(1):269–82.
12. Malta LFB, Caffarena VR, Medeiros ME, Ogasawara T. TA of non-stoichiometric ceria obtained via hydrothermal synthesis. J Therm Anal Calorim. 2004;75:901–10.
13. Aggarwal S, Töpfer J, Tsai T-L, Dieckmann R. Point defects and transport in binary and ternary, non-stoichiometric oxide. Solid State Ionics. 1997;101–103:321–31.
14. Bishop SR, Duncan KL, Wachsman ED. Defect equilibria and chemical expansion in non-stoichiometric undoped and gadolinium-doped cerium oxide. Electrochim Acta. 2009;54(5):1436–43.

15. Hashimoto T, Yoshinaga M, Ueda Y, Komazaki K, Asaoka K, Wang S. Characterization of phase transition of $Ba_{2-x}Sr_xIn_2O_5$ by thermal analysis and high temperature X-ray diffraction. J Therm Anal Calorim. 2002;69:909–17.
16. Vashook VV, Zinkevich MV, Zonov YG, Kharton VV, Tsipis EV, Yaremchenko AA, Marozau IP, Viskup AP, Frade JR, Naumovich EN. Phase relations in oxygen-deficient $SrCoO_{2.5-\delta}$. Solid State Ionics. 1999;116(1–2):129–38.
17. Rycerz L, Ingier-Stocka E, Gadzuric S, Gaune-Escard M. Review of the thermodynamic and transport properties of EuBr2–RbBr binary system. J Therm Anal Calorim 2010. doi: 10.10007/s10973-010-0790-0.
18. Kumekawa Y, Hirai M, Kobayashi Y, Endoh S, Oikawa E, Hashimoto T. Evaluation of thermodynamic and kinetic stability of $CuAlO_2$ and $CuGaO_2$. J Therm Anal Calorim. 2010;99:57–63.
19. Caneiro A, Bonnat M, Fouletier J. Measurement and regulation of oxygen content in selected gases using solid electrolyte cells. IV. Accurate preparation of CO_2–CO and H_2O–H_2 mixtures. J Appl Electrochem. 1981;11:83–90.
20. Caneiro A, Bavdaz P, Fouletier J, Abriata JP. Adaptation of an electrochemical system for measurement and regulation of oxygen partial pressure to a symmetrical thermogravimetric analysis system developed using a Cahn 1000 electrobalance. Rev Sci Instrum. 1982;53:1072–5.
21. Ruddlesden SN, Popper P. The compound $Sr_3Ti_2O_7$ and its structure. Acta Cryst. 1958;11:54–5.
22. Dann SE, Weller MT, Currie DB. Structure and oxygen stoichiometry in $Sr_3Fe_2O_{7-y}$, $0 \leq y \leq 1.0$. J Solid State Chem. 1992; 97: 179–85.
23. Prado F, Armstrong T, Caneiro A, Manthiram A. Structural stability and oxygen permeation properties of $Sr_{3-x}La_xFe_{2-y}Co_yO_{7-\delta}$ ($0 \leq x \leq 0.3$ and $0 \leq y \leq 1.0$). J Electrochem Soc. 2001;148: J7–14.
24. Armstrong T, Prado F, Manthiram A. Synthesis, crystal chemistry, and oxygen permeation properties of $LaSr_3Fe_{3-x}Co_xO_{10}$ ($0 \leq x \leq 1.5$). Solid State Ionics. 2001;140:89–96.
25. Manthiram A, Prado F, Armstrong T. Oxygen separation membranes based on intergrowth structures. Solid State Ionics. 2002; 152–153:647–55.
26. Mogni L, Fouletier J, Prado F, Caneiro A. High-temperature thermodynamic and transport properties of the $Sr_3Fe_2O_{6+\delta}$ mixed conductor. J Solid State Chem. 2005;178:2715–23.
27. Mogni L, Prado F, Caneiro A. Defect structure and electrical conductivity of the Ruddlesden–Popper phases $Sr_3FeMO_{6+\delta}$ (M = Co, Ni). Chem Mater. 2006;18:4163–70.
28. IUPAC. Commission on thermodynamics, oxygen, international thermodynamic tables of the fluid state—9. Oxford: Blackwell Scientific; 1987.
29. Mizusaki J, Mima Y, Yamauchi S, Fueki K, Tawaga H. Nonstoichiometry of the perovskite-type oxides $La_{1-x}Sr_xCoO_{3-\delta}$. J Solid State Chem. 1989;80:102–11.
30. Patrakeev MV, Leonidov IA, Kozhevnikov VL, Kharton V. Ion-electron transport in strontium ferrites: relationships with structural features and stability. Solid State Sci. 2004;6:907–13.
31. Mizusaki J, Yoshihiro M, Yamauchi S, Fueki K. Nonstoichiometry and defect structure of the perovskite-type oxides $La_{1-x}Sr_xFeO_{3-d}$. J Solid State Chem. 1985;58:257–66.
32. Onuma S, Yashiro K, Miyoshi S, Kaimai A, Matsumoto H, Nigara Y, Kawada T, Mizusaki J, Kawamura K, Sakai N, Yokokawa H. Oxygen nonstoichiometry of the perovskite-type oxide $La_{1-x}Ca_xCrO_{3-\delta}$ ($x = 0.1$, 0.2, 0.3). Solid State Ionics. 2004;174:287–93.
33. Mizusaki J, Sasamoto T, Cannon WR, Bowen HK. Electronic conductivity, Seebeck coefficient and defect structure of $La_{1-x}Sr_xFeO_3$ ($x = 0.1, 0.25$). J Am Ceram Soc. 1983;66:247–52.
34. Lankhorst MHR, Bouwmeester HJ, Verweij H. Use of the rigid band formalism to interpret the relationship between O chemical potential and electron concentration in $La_{1-x}Sr_xCoO_{3-\delta}$. Phys Rev Lett. 1996;77:2989–92.
35. Lankhorst MHR, Bouwmeester HJ, Verweij H. High-temperature coulometric titration of $La_{1-x}Sr_xCoO_{3-\delta}$: evidence for the effect of electronic band structure on nonstoichiometry behavior. J Solid State Chem. 1997;133:555–67.
36. Lankhorst MHR, Ten Elshof JE. Thermodynamic quantities and defect structure of $La_{0.6}Sr_{0.4}Co_{1-y}FeyO_{3-\delta}$ ($y = 0$–0.6) from high-temperature coulometric titration experiments. J Solid State Chem. 1997;130:302–302.
37. Van Roosmalen JAM, Cordfunke EHP. A new defect model to describe the oxygen deficiency in perovskite-type oxides. J Solid State Chem. 1991;93:212–9.
38. Kingery WD, Bowen HK, Uhlmann DR. Introduction to ceramics. 2nd ed. New York: Wiley; 1975.
39. Ashcroft N, Mermin N. Solid state physics. Philadelphia: Saunders College; 1976.
40. Raffaelle R, Anderson HU, Sparlin DM, Parris PE. Transport anomalies in the high-temperature hopping conductivity and thermopower of Sr-doped La(Cr, Mn)O_3. Phys Rev B. 1991;43(10): 7991–9.
41. Mott NF. Conduction in glasses containing transition metal ions. J Non-Cryst Solid. 1968;1:1–17.
42. Mogni L, Prado F, Cuello G, Caneiro A. Study of the crystal chemistry of the $n = 2$ Ruddlesden–Popper phases $Sr_3FeMO_{6+\delta}$ (M = Fe, Co, and Ni) using in situ high temperature neutron powder diffraction. Chem Mater. 2009;21:2614–23.
43. Bread Y, Michel C, Hervieu M, Studer F, Maignan A, Raveau B. Large oxygen deficiency in a $n = 2$ member of the RP series: Sr_3FeCoO_{7-x} ($x \leq 1.55$). Chem Mater. 2002;14:3128–35.
44. Viciu L, Zandbergen H, Xu Q, Huang Q, Lee M, Cava RJ. Structure and magnetic properties of the orthorhombic $n = 2$ Ruddlesden–Popper phases $Sr_3Co_2O_{5+\delta}$ ($\delta = 0.91$, 0.64 and 0.38). J Solid State Chem. 2006;179:500–11.
45. Hill JM, Dabrowski B, Mitchell JF, Jorgensen JD. Local defect structure of $Sr_3Co_2O_x$ ($5.64 \leq x \leq 6.60$): evolution of crystallographic and magnetic states. Phys Rev B. 2006;74:174417.
46. Shilova YA, Patrakeev MV, Mitberg EB, Leonidov IA, Kozhevnikov VL, Poeppelmeier KR. Order–disorder enhanced oxygen conductivity and electron transport in Ruddlesden–Popper ferrite-titanate $Sr_3Fe_{2-x}Ti_xO_{6+\delta}$. J Solid State Chem. 2002; 168:275–83.
47. Markov AA, Patrakeev MV, Kharton VV, Pivak YV, Leonidov IA, Kozhevnikov VL. Oxygen nonstoichiometry and ionic conductivity of $Sr_3Fe_{2-x}Sc_xO_{7-\delta}$. Chem Mater. 2007;19:3980–7.